Shock-Wave/Boundary Layer Interactions Induced by a Cylinder Spanning a Gap

Layton W. Howerton*, Gregory A. Blaisdell†, and Jonathan Poggie‡
Purdue University, West Lafayette, Indiana 47907

Improved delayed detached eddy simulation (IDDES) is applied to a cylinder located between flat plates in Mach 5.95 flow. Reynolds-averaged Navier-Stokes (RANS) calculations were completed for comparison to the IDDES time-averaged flow. The geometry represents a simplification of the gap between a missile and fin with a connecting cylinder, or torque tube. The cylinder diameter is approximately twice the gap height between the flat plates for the configuration tested. Experimental results from the Arnold Engineering Development Center from 1979 are used for comparison. Continuing from past work on this geometry with RANS and IDDES, differences between the current and previous approaches are highlighted. The primary difference is that the inflow boundary condition has been changed from uniform flow to a developed boundary layer profile. The heat flux, pressure, and skin friction are calculated on the plates and cylinder and compared. Unsteady shock-wave/boundary-layer interactions are evaluated with a time-accurate IDDES method. Power spectral densities of time history data are calculated and compared. Shock-wave/boundary-layer interactions can produce areas of high pressure and heat transfer. These areas are then compared with experimental data and previous computational work. Computationally evaluating shock-wave/boundary-layer interactions can provide valuable quantitative and qualitative assessments to be used in ground testing and flight vehicle design.

Nomenclature

C_f	=	skin friction coefficient
CFL	=	Courant-Friedrichs-Lewy number
D	=	cylinder diameter
f_s	=	sampling frequency
g_h	=	gap height
h	=	heat transfer coefficient
M	=	Mach number
P	=	pressure
$\dot{q}$	=	heat flux
Re	=	Reynolds number
T	=	temperature
t	=	time
Δs	=	first cell wall-normal grid spacing
$\Delta(x, y, z)^+$	=	nondimensional coordinates in viscous wall units
ν	=	kinematic viscosity
τ	=	shear stress
$()_{ref}$	=	reference property
$()_w$	=	wall property
$()_\infty$	=	freestream property
$()_0$	=	stagnation property

*Graduate Student, School of Aeronautics and Astronautics, AIAA Student Member.
†Professor, School of Aeronautics and Astronautics, AIAA Associate Fellow.
‡Professor, School of Aeronautics and Astronautics, AIAA Associate Fellow.

I. Introduction

Often overlooked geometric imperfections, like gaps and cavities, must be fully understood to complete comprehensive aerothermodynamic design and analysis of an aerospace vehicle. While the idealized smooth outer mold line on aerospace vehicles likely dominates the global aerodynamic characteristics, locations such as gaps and cavities have the potential to cause significant issues at high speeds. Prevailing research into these geometric imperfections have shown high heating [1, 2]. The shock-wave/boundary-layer interactions can be quite complex in gap regions as previous work on this geometry demonstrated [3]. Continued research into shock-wave/boundary-layer interactions in gaps will improve the collective understanding as to how the shock-wave/boundary-layer interaction, which is an established unsteady source of increased heating and pressure [4, 5], can change given the bounding nature of gap regions on a realistic vehicle geometry. A complex series of reflecting shock-wave/boundary-layer interactions was seen in [3] as well as the current work.

The geometric configuration used is a simplified representation of the experimental setup of Neumann and Hayes [6] and recent calculations using RANS simulation by Alviani et al. [7]. Most recently, the RANS and IDDES simulations in Howerton et al. [3] are the groundwork for the current simulations. The cylinder in this work represents the torque tube which, in the Neumann and Hayes experiment, connected a generic ogive-cylinder missile body to a fin. The gap created between the body of the missile and the fin is the geometry of interest. While the entire body is not being simulated, a boundary layer profile which matches the experimental boundary layer thickness is applied at the inflow improving the ability to compare with the experimental data. The previous simulations in Howerton et al. used a uniform inflow boundary condition set to freestream conditions. The different inflow boundary condition is the primary change to the current work. The dramatic difference in heating between the the previous work in [3] and the current work illustrates the importance, from a design perspective, of whether a gap will experience a flow much more similar to freestream conditions or be immersed and shielded, to an extent, in a developed supersonic boundary layer. Future designs for high-speed vehicles may need to consider such variations in heating as the conditions in a gap may change with aerodynamic factors like angle of attack.

The simplification of the top and bottom surfaces being represented as wide flat plates is an idealization, but the focus of the present analysis is on centerplane heating and pressure on the upstream side of the cylinder compared to previous computation and experiment. The computational domain is shown in Fig. 1. The cylinder is shown in yellow. The plates are shown in gray. The bottom plate will represent the missile body and is located in the $y = 0$ m plane. The top plate represents the underside of the fin, and is located in the $y = 0.00762$ m plane. The gap height is defined as $g_h = 7.62$ mm; the distance between the upper and lower plate. The inflow plane is blue. The sidewalls are purple, and the outflow plane is hidden in Fig. 1. The cylinder diameter is $D = 15.9$ mm. The gap height and diameter studied here were previously used in [3, 6, 7]. Figure 2 highlights the location of the gap region on the missile-fin configuration tested experimentally by Neumann and Hayes. The missile-fin geometry shown in Fig. 2 comes from the computational work of Alviani et al. [7]. The cylinder diameter is used for nondimensionalization. The inflow plane is the same distance upstream as the experimental fin tip. At that station along the ogive-cylinder with the fin removed, the experiment found a boundary layer thickness greater than the g_h used in this calculation. Thus, only a portion of the boundary layer enters the gap region. An auxiliary RANS simulation was created to generate the inflow boundary layer profile for the IDDES domain. An iteratively and grid converged set of RANS simulations with the same boundary conditions is used throughout as a comparison for the IDDES calculation.

The outline of the paper is as follows. Section I provides an introduction and motivation for the research. Section II describes the methodology used for computational meshing and solver configurations. Section III examines the computational results. Section IV summarizes and concludes with notes for future avenues of work.

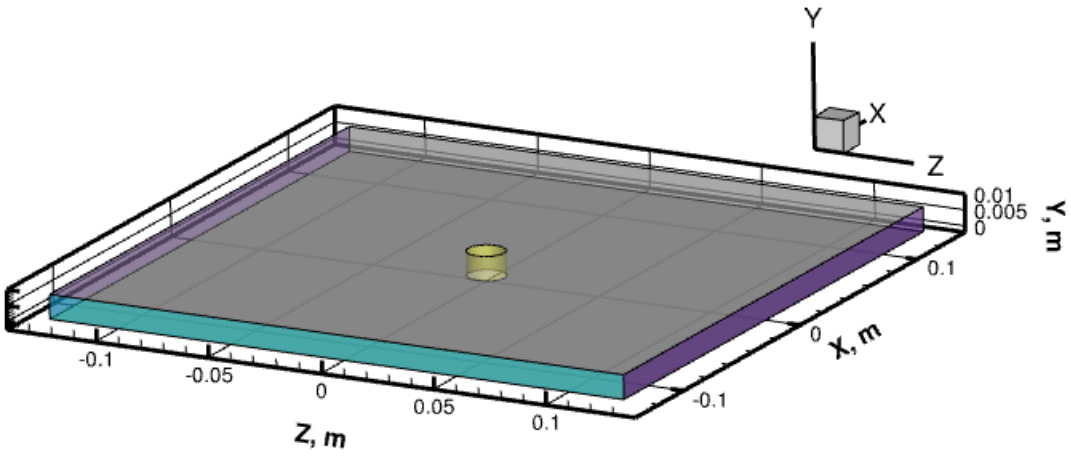

Fig. 1 Computational domain.

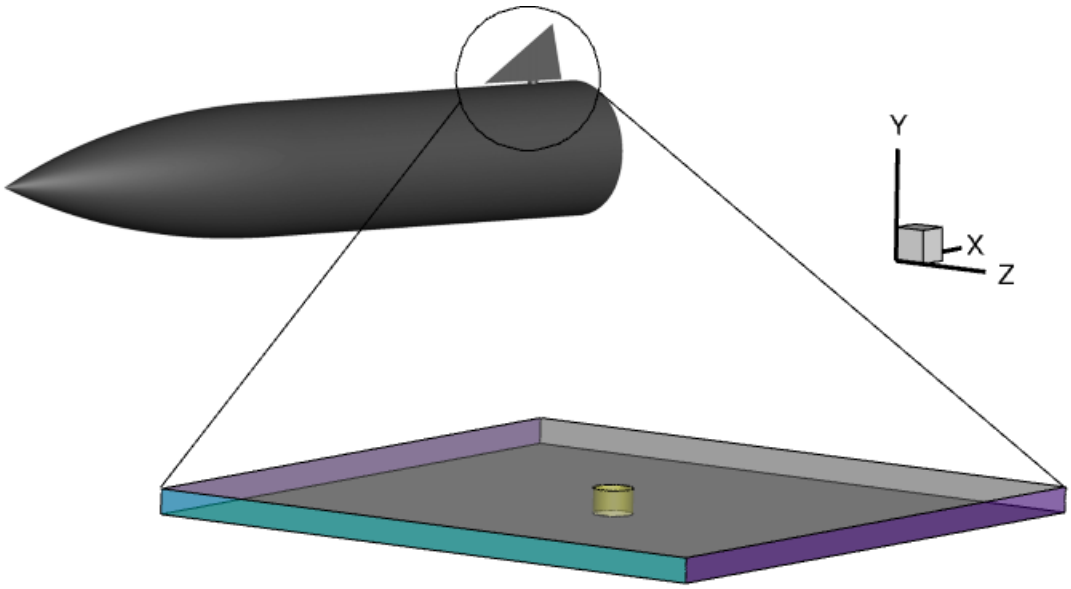

Fig. 2 Missile-fin orientation and simplification.

II. Methodology

Computational grids were generated with the Pointwise grid generation software [8]. Post-processing computational data was completed with Tecplot [9] and MATLAB software [10]. CREATE-AV Kestrel is the Department of Defense computational fluid dynamics package [11] used for the present work and in the previous work in Howerton et al. [3]. The Kestrel computational fluid dynamics (KCFD) solver is the portion of the CREATE-AV software package used for the simulations discussed. KCFD uses a finite-volume, unstructured, cell-centered method. The Harten-Lax-van Leer-Einfeldt (HLLE++) method was employed for inviscid flux calculation. The viscous flux scheme used was the alpha-damping method. Van Leer's scheme was used for the calculation of convective flux Jacobians. The Kestrel

CFD package has a flux limiter called Kestrel+ which was used. The simulations were run using second-order accuracy spatially and temporally. The second-order accuracy in time relied on a subiterative point-implicit scheme [12]. Three subiterations were completed during each time step. The Splart-Allmaras (SA) turbulence model was used. KCFD was used in the improved delayed detached eddy simulation (IDDES) mode to investigate unsteady motion in the shock-wave/boundary-layer interaction. For the RANS calculations, the CFL number has been left at the default value of 1000.

The wall boundary condition used for both plates and the cylinder was isothermal no-slip surface at T_w = 300 K. The inlet condition was set to the boundary layer profile file which was created with a precursor RANS simulation. The velocity profile for the incoming boundary layer profile is shown in Fig. 3. The boundary layer applied at the inflow is an approximation of the boundary layer which was measured experimentally without presence of the fin. In Fig. 4 the normalized total pressure profiles through the boundary layer are shown for the experimental and imposed boundary condition. As can be seen from the horizontal lines, slightly less than half of the boundary layer is ingested into the gap. The experimental boundary layer thickness from the work of Neumann and Hayes [6] for the presented case is 16 mm. While the total pressure profiles disagree, only two data points can be directly compared. The auxiliary RANS solution which produced the boundary layer profile was generated by matching the experimental boundary layer thickness on a flat plate developed from zero thickness. There is an assumption by choosing this computationally efficient route that the profile would be similar to that which developed on the experimental ogive. Future research could be done to evaluate this assumption in this context. The outflow boundary coundition was extrapolated. The spanwise boundary conditions were symmetry.

For the IDDES runs, the time step used was $\Delta t = 1 \times 10^{-7}$ s. Time histories at points of interest were sampled at f_s = 10 MHz which corresponds to every computational time step. Planar cuts along the centerline upstream of the cylinder and all model surfaces were sampled at f_s = 10 kHz. Full volume solutions were collected at f_s = 1 kHz. Roughly 340,000 time steps were completed for the IDDES simulation which corresponds to 34 ms of physical time. Computational resources for these simulations were provided by the Navy DoD Supercomputing Resource Center HPE Cray EX system, Narwhal. Narwhal uses AMD Epyc ROME 7H12 processors which are clocked at 2.6 GHz. Each Narwhal node has two 64-core processors, and 50 Narwhal nodes were used for these computations. Freestream conditions are listed in Table 1.

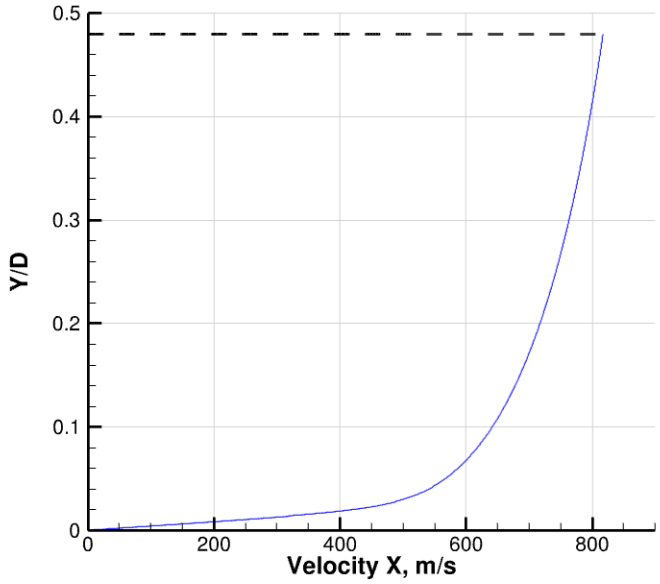

Fig. 3 Incoming boundary layer velocity profile (dashed line represents top wall).

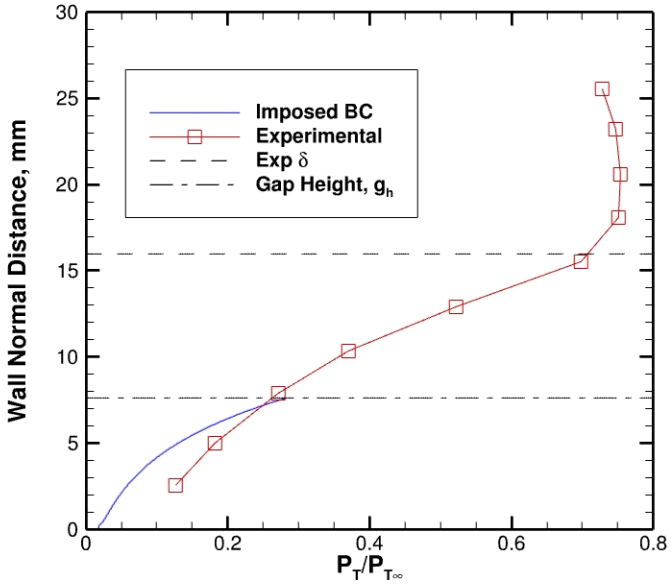

Fig. 4 Incoming boundary layer normalized total pressure profile compared with experimental data.

Table 1 Freestream flow conditions

Parameter	Value
M_∞	5.95
ρ_∞	0.07017 kg/m^3
P_∞	1149 Pa
T_∞	57.06 K
μ_∞	3.753×10^{-6} Pa · s
u_∞	900.9 m/s
$P_{0\infty}$	1.724×10^6 Pa
$T_{0\infty}$	461.1 K
Re_∞	1.685×10^7 m^{-1}

A. Computational Mesh

All grids created are fully structured. For the RANS simulations, a coarse, medium, and fine grid were used for grid independence studies. Iterative convergence was confirmed for all three RANS grids. The coordinate system for the grid is centered at the center of the cylinder on what will be described as the bottom, $y = 0$, wall. The x,y, and z directions correspond to streamwise, wall-normal, and spanwise directions. The dimensions of the computational domain were: -0.1272 m< x <0.1272 m, 0 m< y <0.00762 m, and -0.1272 m< z <0.1272 m. For the IDDES grid, the same grid strategy was use as in Howerton et al. [3]. A radially aligned grid of LES quality cells surrounded the cylinder with a buffer of RANS quality grid outside of the LES quality grid. The two regions can be visualized in Fig. 5 (b). In Fig. 5 (a) the grid is shown for the centerplane, every other grid line has been removed for both Fig 5 (a-b). The IDDES grid contains roughly 220 million cells.

All grids were created such that $\Delta y_w^+ \leq 1$ in attached boundary layers. The RANS grids were 0.6, 3.5, and 21 million points respectively. The primary difference between the RANS grids of the current work and those used in [3] was the additional use of the Pointwise smoothing feature using the Steger-Sorenson boundary control function to lower

maximum included angles and smooth grid block transitions. The IDDES grid is the same as was used in this group's previous work in reference [3]. The IDDES grid LES quality cells are approximately uniform away from the wall with inner coordinates of $\Delta x^+ \approx 40$, $\Delta z^+ \approx 23$, and $\Delta y^+ \approx 4$ while at the wall the spacing decreases to $\Delta y_w^+ \leq 1$. The values where chosen based on recommendations for wall-resolved LES of turbulent boundary layers [13]. The outer RANS quality portion of the IDDES grid had approximately the same grid resolution with a slightly smaller first point wall spacing of Δs of 1.5×10^{-6} m to match the Δy_w^+ achieved in the LES quality region. The transition between the regions occurred at $x/D = 5$. This choice kept the separation upstream of the cylinder entirely in the LES quality region. Of the 220 million cells that make up the IDDES grid, 203 million are within the LES quality grid region. A plot of the centerline values of nondimensionalized time step ($\Delta t^+ = (\tau_w/\rho_w)\Delta t/\nu_w$) and Δy_w^+ are shown in Fig. 6. The peaks that occur very near the cylinder wall junction at $x/D = 0.5$ will be shown later to occur within a recirculation region.

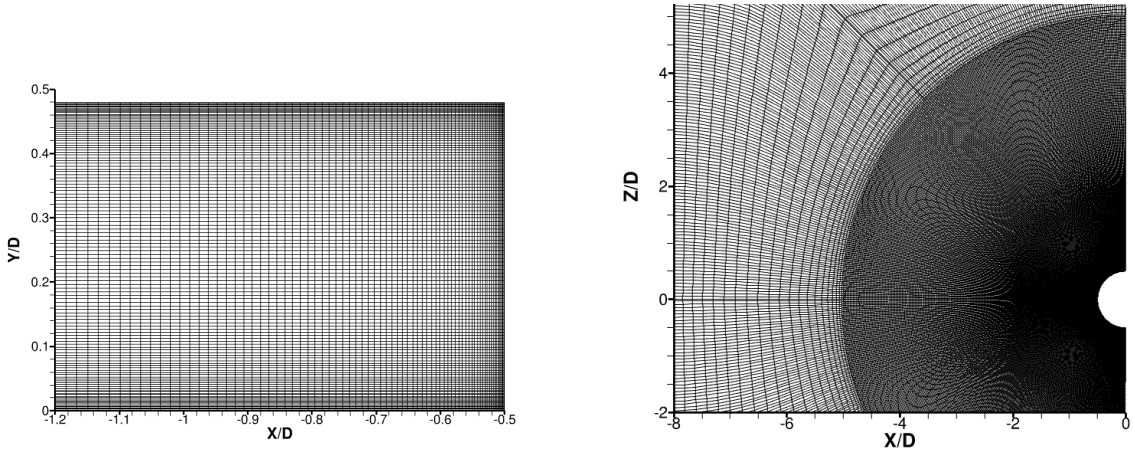

(a) $z = 0$ plane

(b) $y = 0$ plane

Fig. 5 IDDES Computational grid in SWBLI region. Every other grid point plotted for clarity.

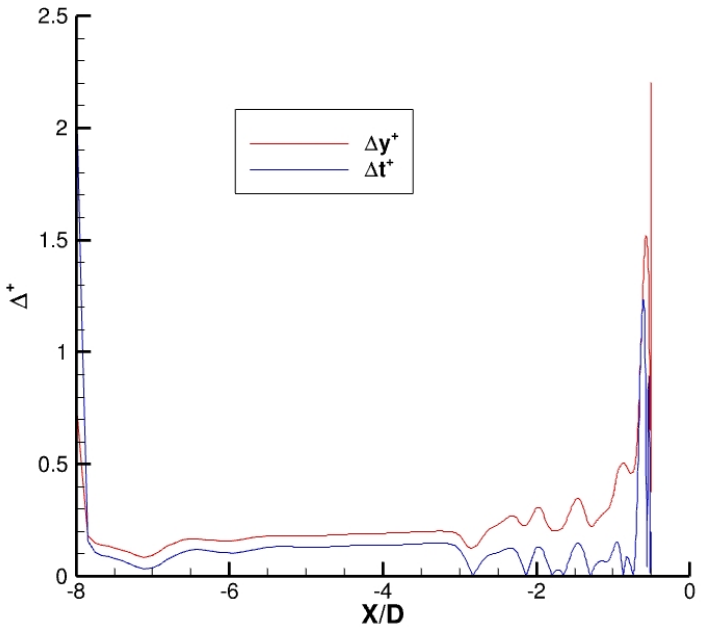

Fig. 6 IDDES nondimensionalized wall normal grid spacing and time step along top plate centerline ($z = 0$)**.**

III. Results

To begin to quantitatively and qualitatively describe the IDDES and RANS simulations, RANS simulations are discussed first. Then the IDDES results are presented, and all simulations are compared with each other and the previous experimental and computational work. In the previous computations of Howerton et al. [3] in which the gap was presented with freestream conditions, the shock train in front of the cylinder displayed a significant streamwise motion. In the current work, the amplitude of the unsteady streamwise shock motion is smaller and closer to that seen in blunt fin simulations such as those completed by Ngoh and Poggie [14, 15]. Other similarities and differences are discussed such as the trends of surface pressure and heat transfer.

Shock-wave/boundary layer interactions and the associated unsteadiness have been a recent focus of the aerospace community. At high speeds, the flow unsteadiness can cause unsteady thermal and pressure loading. Surface pressure and heat transfer will thus be the driving parameters considered here. Many studies and review articles [4, 5, 16] discussing shock-wave/boundary layer interactions emphasize the importance of the low frequency component of the unsteady interaction. To investigate the unsteady features of this flow, power spectral density analysis is employed to evaluate the frequency content in the flow at several locations of interest.

A. RANS Results

Each grid refinement level, coarse, medium and fine, was independently evaluated for iterative convergence. Quantities of interest were tracked and percent changes across intervals of 10k iterations until the change was of the order of 0.1 percent between subsequent intervals. All solutions shown are iteratively converged. The iteratively converged solutions on each grid were then evaluated against each other across several key quantities of interest. Streamwise skin friction coefficient, surface pressure, and heat transfer coefficient were evaluated. A representative evaluation between grids is shown in Fig. 7. The maximum change in the solution for the quantities of interest within the area of interest was less that 3% between the medium and fine RANS solutions. Accepting the RANS solution to be iteratively and grid converged, the fine grid RANS solutions will be presented. The heat transfer coefficient [17] is defined here as

$$h = \frac{\dot{q}_w}{0.9T_{0\infty} - T_w} \tag{1}$$

with $\dot{q}_w$ as wall heat flux per unit area in W/m^2, T_w as wall temperature in K, and $0.9T_{0\infty}$ being a reference value in K. This reference was chosen for consistency with previous studies [3] [6] [7] .

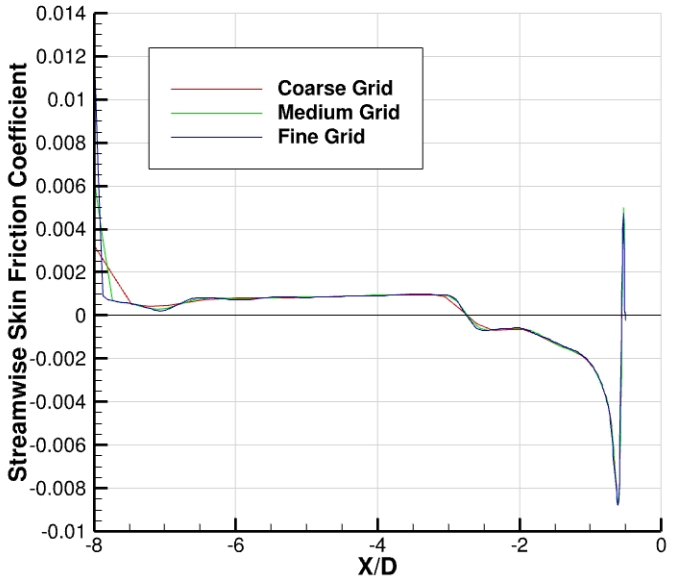

Fig. 7 RANS C_{fx} Streamwise skin friction coefficient centerline bottom plate, including grid convergence.

The streamwise skin friction coefficient taken from the centerline upstream of the cylinder on the top and bottom wall is shown in Fig. 8. Both curves have peaks at the left edge where the inflow boundary condition is imposed and the top and bottom no-slip walls meet. The values for both top and bottom wall stabilize to nearly constant streamwise skin friction coefficient. The influence of the bluff body creates a bow shock upstream. As an indication of a possible separation, C_{fx} becomes negative first on the bottom wall at $x/D = -2.77$ then on the top wall at $x/D = -2.29$. Here the flow along the top wall reattaches at $x/D = -1.91$, while the flow along the bottom wall remains separated. The flow along the top wall separates a second time at $x/D = -1.05$ and remains separated. To verify qualitatively in this context that the negative C_{fx} can be used to identify separation and reattachment points, Fig. 9 shows Mach number contours in the centerplane upstream of the cylinder from $x/D = -3.5$ up to the cylinder face. The streamlines overlaid on the Mach number contours shows that the bottom wall first develops a large separation bubble. The shock which occurs at this separation impinges on the top wall. At the shock impingement, the flow briefly separates as shown by the small recirculation bubble is seen on the top wall near $x/D = -2.1$. An additional recirculation occurs near the junction of the cylinder with the top wall, and this structure is associated with the negative skin friction region seen in Fig. 8 near $x/D = -1$. Finally a very small vortex is shown in the junction of the bottom wall with the cylinder. The flow very near the cylinder is primarily flowing in the y direction and, as this flow reaches the bottom wall, some of streamlines join the largest recirculation and move upstream while a small portion moves downstream towards the wall-cylinder junctions. A closer inspection of the skin friction coefficient very near the cylinder junction shown in Fig. 10 shows an additional pair of C_{fx} sign changes, indicating additional small vorticies. This is verified in Fig. 11 with streamlines highlighted to show the described behavior. Flow streamlines in Figure 18 from Alviani et al. [7] are quite similar to those seen in Fig. 9. This is qualitatively promising due to the simplifications of the geometry made in this work.

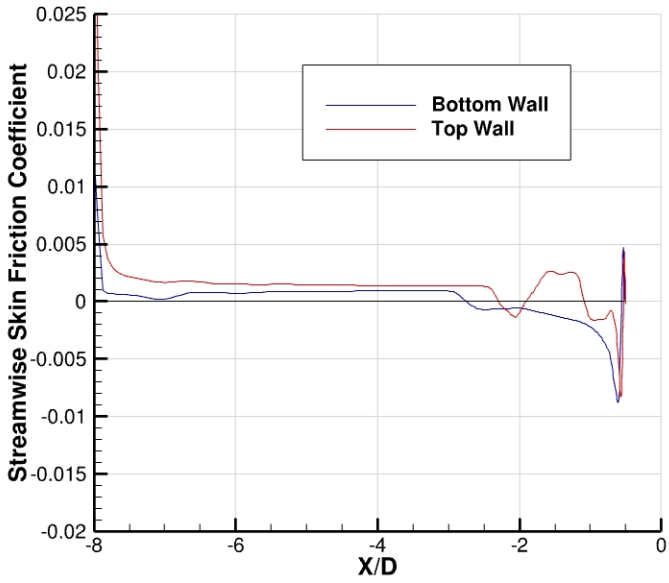

Fig. 8 RANS C_{fx} Streamwise skin friction coefficient centerline.

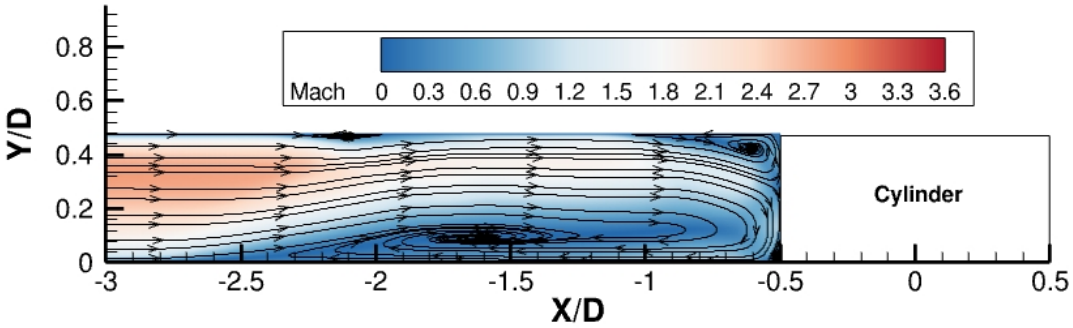

Fig. 9 RANS centerline plane Mach number with streamlines.

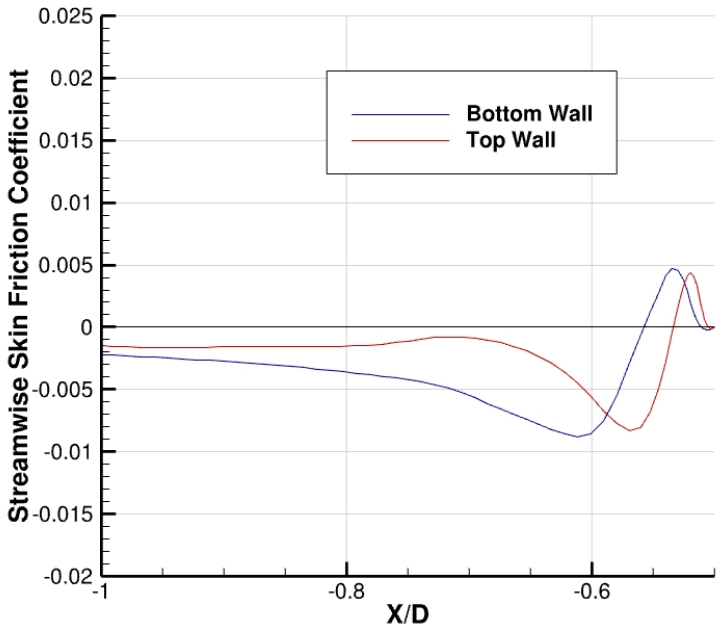

Fig. 10 RANS C_{fx} Streamwise skin friction coefficient centerline, expanded axis.

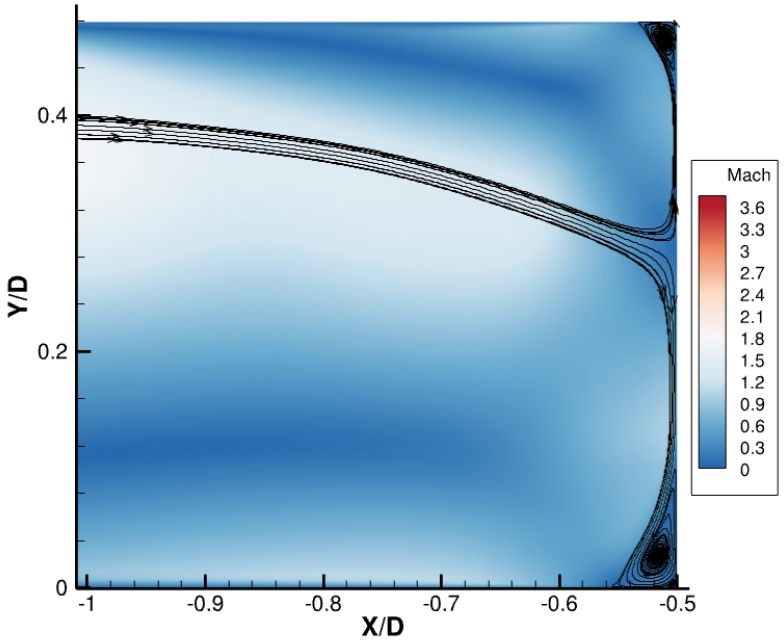

Fig. 11 RANS centerline plane Mach number with selected, expanded axis.

Heat transfer rates and surface pressure loads can increase significantly with shock-wave/boundary-layer interactions [3, 7, 18]. The complex interaction which has just been described produces many instances of separation and reattachment.

The resulting system of shocks is quite complex. Figure 12 shows the wall static pressures normalized by the freestream static pressure on the top and bottom wall on the centerline upstream of the cylinder. A slight increase on the bottom wall curve can be seen near the location of the first separation on that wall because the flow downstream of that point will have passed through the separation shock. The peak pressure on the bottom wall occurs at $x/D = -0.56$. Referencing that location back to Fig. 11, it can be inferred that the peak pressure is associated with the impinging streamlines attaching to the wall at the upstream edge of the small vortex. The pressure spikes seen in the top wall correspond to the x/D where the shock-wave/boundary-layer interactions were shown in the plot of streamwise skin friction coefficient. The peak values for pressure are both greater than 10 times higher than the freestream static pressure. The work of Alviani et al. [7] completed RANS simulations of the entire missle geometry and for the same conditions as those shown in Fig. 12 they obtained a value of $P_w/P_\infty = 9$. The peak normalized pressures of a similar order contrast to the previous work in Howerton et al. [3] in which freestream conditions were applied at the inflow. With the freestream conditions as an inflow a peak value of $P_w/P_\infty = 55$ was found. It was posited in [3] that multiple factors were causing the high pressures, including the higher inflow Mach number and the lack of three-dimensional relieving effects which a curved missle body allows for compared to the current idealized configuration. This result may indicate that it was primarily the boundary condition causing the difference. Localized pressure peaks ten times higher than other nearby areas could cause a vehicle to fail if not accounted for.

For a comparison to traditional supersonic blunt fin flows, the works of Dolling and Bogdonoff [19, 20] and Ngoh and Poggie [14] are included in Fig. 13. The experiments of Dolling and Bogdonoff were completed in the Princeton University 8-in.-by-8-in., supersonic blow-down tunnel. The freestream Mach number in the experiment was 3. The Mach number at the top edge of the profile being prescribed as an inflow to the current simulations, seen in in Fig. 3, is roughly Mach 3.5. While the flow conditions differ, the comparison illustrates the difference between the gap geometry and a blunt fin. The work of Ngoh and Poggie [14] simulated the Dolling and Bogdonoff experimental conditions using detached eddy simulation. The incoming turbulent boundary layer in the experiment was 3.3 mm. The comparison data was re-normalized by the cylinder diameter used in the present simulations. Only the bottom wall is compared as the top wall does not exist in the context of the Dolling and Bogdonoff configuration. It can be seen that the flow constraining effect of the gap region moves the pressure rise upstream. The characteristic feature of the relatively small pressure rise and fall followed by a peak near the bluff body seen in all of the traditional blunt flow data is not present in the gap case. The cause is likely due to the reflected shock coming from the top wall and interacting with the growing separation bubble on the bottom wall. In comparison to Figure 8 of Ngoh and Poggie [14], one can see that the impingement of the separation shock on the inviscid bow shock is roughly one blunt fin diameter above the wall-fin juncture. The present simulations have a gap height slightly less than one half of a cylinder diameter. The geometry constrains the flow and changes the interaction. The reflection of the furthest upstream separated shock back into the recirculation region causes higher pressures than traditional blunt fin flows. The peak pressure value for the RANS bottom wall is on the order of twice the result from Ngoh and Poggie IDDES.

The heat transfer coefficient along the top and bottom walls are shown in Fig. 14. The pattern of peaks and valleys follows the same pattern as wall pressure. The reattachment points specifically experience very large peak heat transfer rates. The heat transfer at the inflow boundary condition is initially very high and quickly stabilizes to near the expected value which is the reference heat transfer coefficient taken from the Neumann and Hayes experimental data [6]. The reference value for heat transfer coefficient was collected without the fin installed in the experiment, and is $h_{ref} = 26\ W/(m^2K)$. The heat transfer peaks at $h/h_{ref} = 33$ on the bottom wall. In Alviani et al., the peak heat transfer coefficient for the same geometry was $h/h_{ref} = 20$. However, as can be seen from the experimental data, the peak measured was $h/h_{ref} = 7$. Importantly, the closest experimental data point to the cylinder misses the peak heating very near the juncture of the wall and the cylinder. This result is confirmed in the previous computations for this work by Howerton et al. and Alviani et al. [3, 7]. At the closest experimental station, $x/D = -0.8$, the bottom wall heat transfer coefficient is $h/h_{ref} = 7.5$ which is in reasonable agreement with the experiment. Evaluating the global simulation peak wall heat transfer coefficient turns the attention to the stagnation point on the cylinder leading edge which was illustrated with streamlines in Fig. 11. While there was no experimental data taken on the cylinder, the current RANS simulation as well as all previous known simulations of this specific configuration found the highest heat transfer coefficient on the cylinder leading edge. Figure 15 shows the heat transfer coefficient on the leading edge of the cylinder. The peak value occurs at $y/D = 0.29$ and is equal to $h/h_{ref} = 45.5$. Referencing again to Fig. 11, qualitatively the streamlines appear to impinge at the same y/D value. Alviani et al.[7] found a maximum heat transfer of $h/h_{ref} = 23$ at the cylinder stagnation point for this geometry. The flow stagnation in that region of the cylinder increases the heat transfer and pressure well above other areas of the flow. Accounting for stagnation point heating in gaps should not be neglected for high speed vehicles.

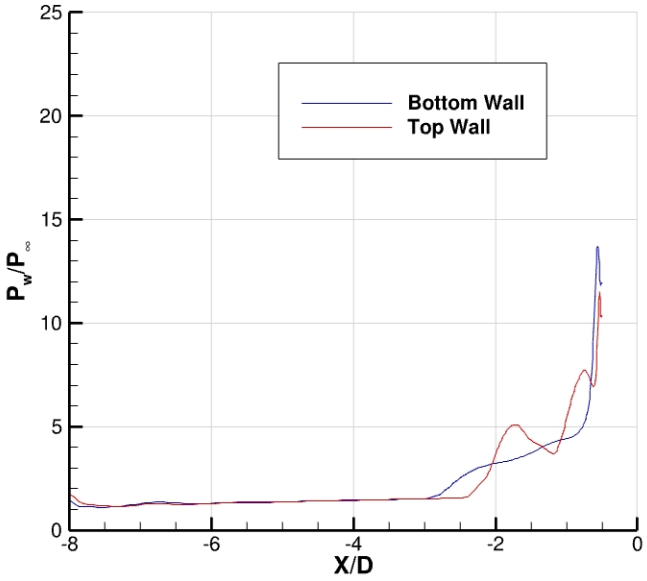

Fig. 12 RANS pressure centerline.

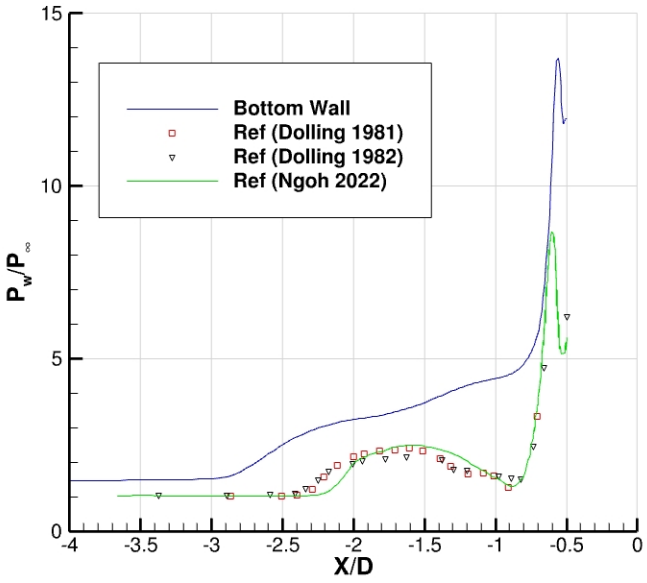

Fig. 13 RANS pressure centerline bottom wall including experimental and computational data.

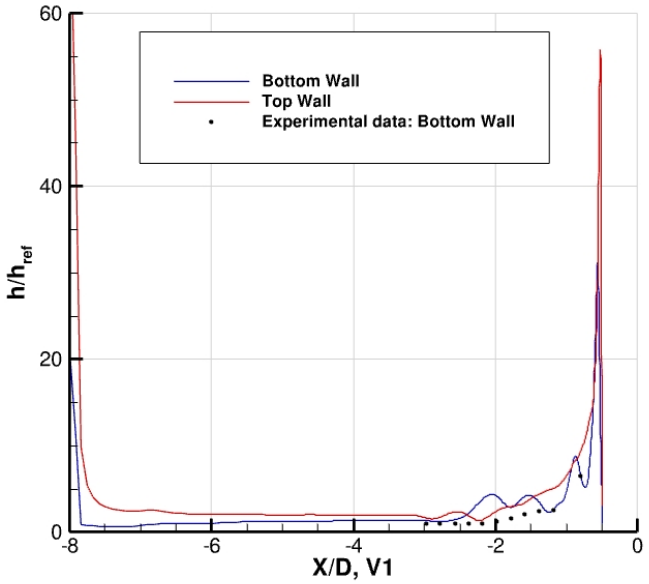

Fig. 14 RANS heat transfer coefficient centerline.

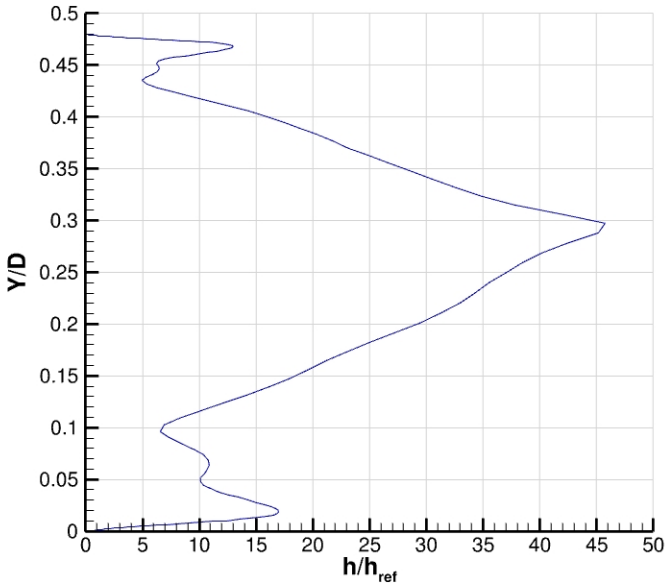

Fig. 15 RANS heat transfer coefficient on cylinder leading edge.

B. IDDES Results

Time-averaged Mach number contours are shown in Fig. 16 to Fig. 18. Figure 16 shows the top-down view of the domain with the cylinder located in the center of the contour. This plane is halfway between the flat plates and shows several of the interesting features of the flow. Behind the first bow shock, there is a pattern of increased and decreased Mach number. This pattern can also be visualized in the Mach number contour in the centerline plane in Fig. 17. This

pattern is due to the bounded nature of the flow in the y direction. In a typical blunt fin flow, the flow is not bounded in the y-direction near the wall-fin juncture, but here, the furthest upstream separating shock-wave is now reflected off of the top wall. Qualitatively comparing the Mach number contours indicates a different possible configuration of shock strengths and separation bubbles. More shock reflections, relative to the RANS simulation, appear to create a more well-defined supersonic jet between complex vorticies. Shocks from both walls continue to interact in a narrowing region with separated flow on both walls before the jet impinges on the cylinder surface. Streamlines in Fig. 18 shows the recirculation of a large separated region on the top wall. Note the largest separation was on the bottom wall in the RANS simulations. The streamlines also illustrate the impingement into the cylinder and provide a qualitative y/D location for investigation of stagnation point heating. The bottom wall shows smaller separation regions and Fig. 19, showing skin friction coefficient on the top and bottom walls upstream of the cylinder, gives further insight to the separation and reattachment behavior. Interestingly, the flow separates from the bottom wall several times before reaching to the wall. This is likely due to the reflecting shock-waves impinging at the wall and causing relatively small separation bubbles that reattach. The top wall curve shows that the flow does not reattach after separating the first time. Figure 20 shows the first quadrant of the bottom wall surface colored by the magnitude of skin friction coefficient. The outline of the cylinder is included for reference. The lines on the surface represent the trajectories of the skin friction vector field on the surface. The alternating pattern of converging and diverging streamlines represents locations where the flow is separating and reattaching to the surface. A line which has vectors converging towards it represents a location which the flow is separating up off the surface, and diverging streamlines represent the flow impinging onto the surface at a reattachment point. The separation and reattachment streamlines are illustrated by the sign changes on the centerline streamwise skin friction coefficient shown in Fig. 19. Approaching the cylinder, the space between successive separation and reattachment lines shrinks.

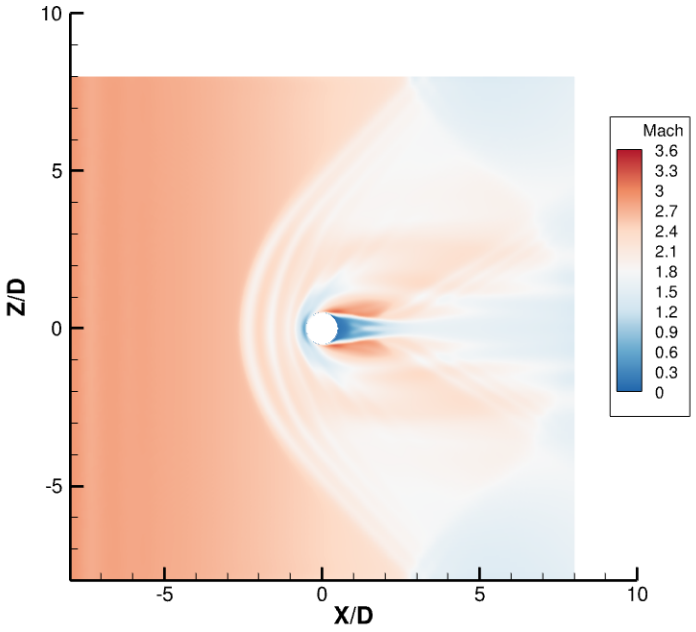

Fig. 16 IDDES y = 0.00381 plane mean Mach number.

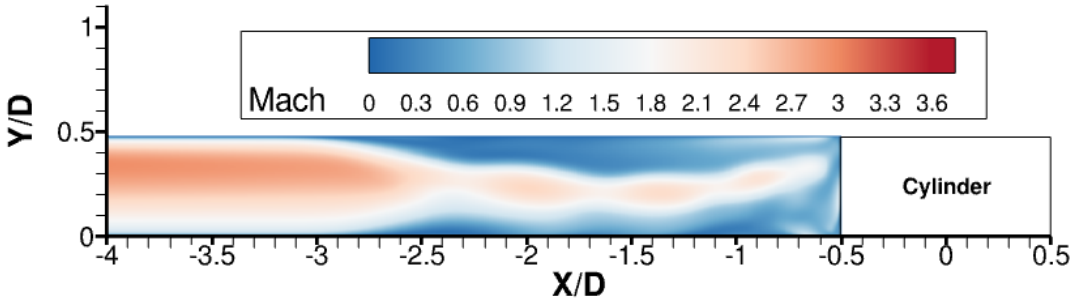

Fig. 17 IDDES centerline plane mean Mach number.

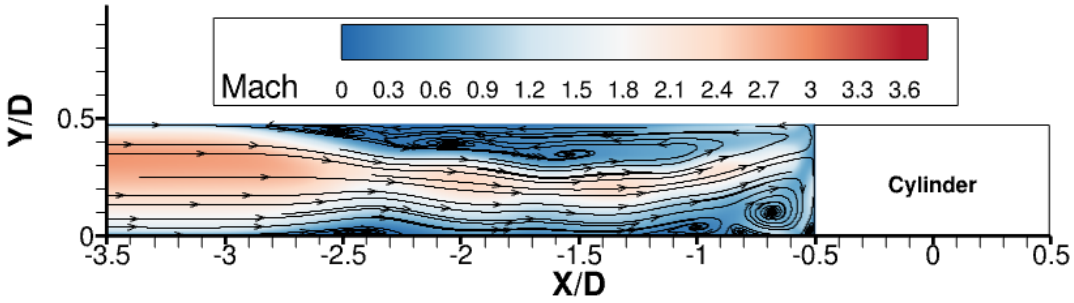

Fig. 18 IDDES centerline plane mean Mach number with velocity streamlines.

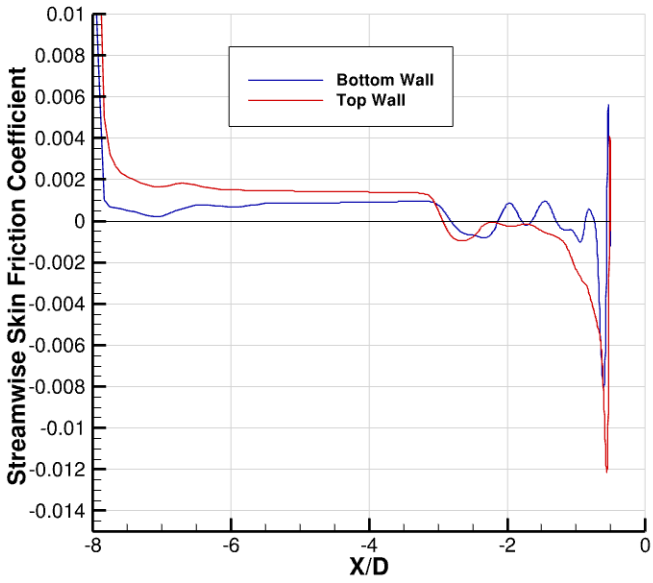

Fig. 19 IDDES C_{fx} time-averaged streamwise skin friction coefficient, centerline top and bottom plate.

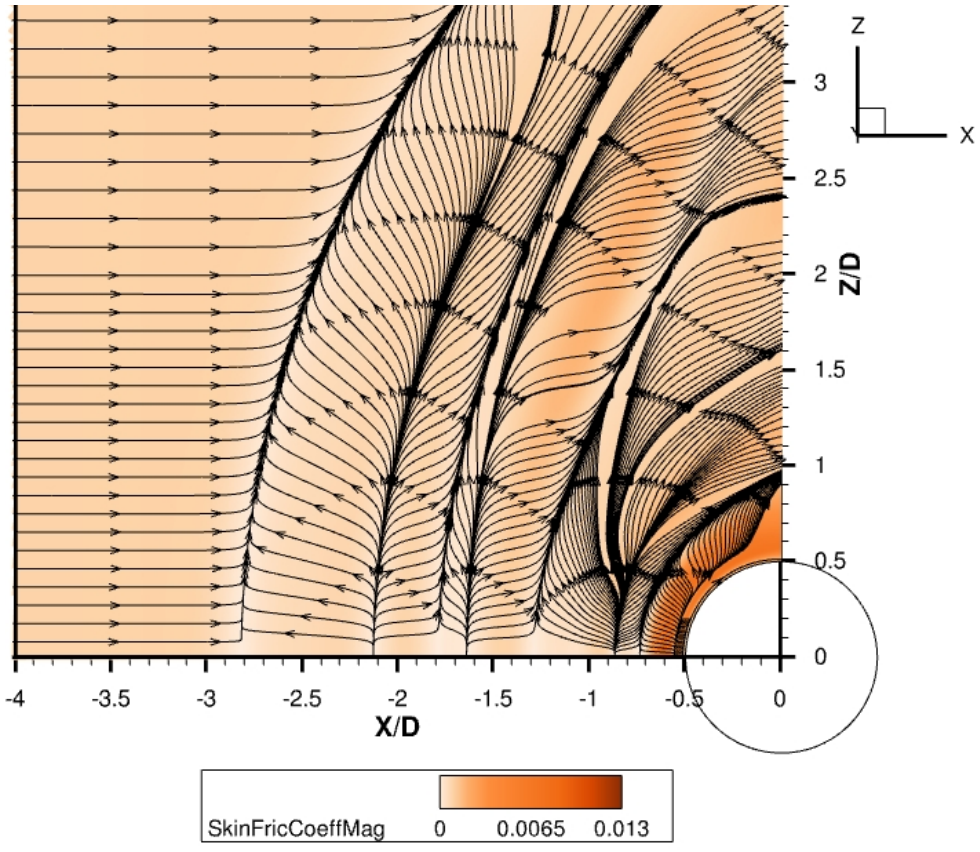

Fig. 20 IDDES C_f magnitude contour and skin friction coefficient trajectories, bottom plate.

The pressure and heat transfer on the centerline are shown in Fig. 21 through Fig. 23. The pressure rise from the shock-wave/boundary-layer interactions can be seen in both the top and bottom wall. The top wall only has one primary increase before slightly decreasing in the separated region. However, the bottom wall has several smaller increases after the first primary increase. Looking at the locations compared with the skin friction and Mach number contours seen in Fig. 19 and Fig. 18, the smaller increases in pressure likely are due to the additional interactions due to the reflected shocks. Recalling Fig. 12, it was the bottom wall which had one primary increase before reaching the spike. This behavior is seen in other blunt body simulations [14]. The pressures spike for both walls as they reach the cylinder. This behavior also occurs in the RANS, but the peak values between top and bottom wall in the RANS are much more similar in magnitude compared to those in Fig. 21. The top wall in the IDDES experiences a peak pressure greater than two times larger than the bottom wall. The difference might be the relative location of the impingement of the supersonic jet which is maintained between the separated walls. Seen in Fig. 18, the impingement is much closer to the top wall junction compared to the bottom wall junction. In the RANS simulation, the location was roughly $y/D = 0.3$, but Fig. 18 shows a value closer to $y/D = 0.35$. Figure 22 shows a similar comparison of pressure rise along the wall to the experiments of Dolling and Bogdonoff made previously for the RANS simulations. Similar to the RANS comparison, the IDDES of the gap configuration shows the pressure rise begins further upstream, does not display the traditional blunt fin double peak pressure profile, and has a higher peak than the blunt fin configuration. However, the IDDES peak value is much closer compared to the DES completed in Ngoh and Poggie [14]. Further research may need to be conducted to determine reasons for the peak pressure discrepancies between IDDES and RANS methods discussed here and in the previous work in Howerton et al. [3].

Along with the pressure rise, heat transfer also rises dramatically at the cylinder junction in Fig. 23. Small bumps between $x/D = -3$ to $x/D = -1$ in the heat transfer plot on the lower wall are likely due to the heating associated with reattachment as the flow separates and reattaches to the bottom wall several times before reaching the cylinder junction. The high heat transfer at the inflow plane, particularly at the top wall, is likely due to the sudden growth from zero boundary layer thickness on the top wall at what would be the leading edge of the missile fin. Those values are also likely affected by the imposed boundary layer profile at the inflow boundary condition. Similar to the trend seen in the pressure profiles, the top wall heat transfer is also much higher compared to the bottom wall. The RANS peak heat transfer coefficients were both roughly $h/h_{ref} = 33$. For the IDDES the bottom wall remained at a similar level near $h/h_{ref} = 30$, but the top wall value reached $h/h_{ref} = 55$. Unlike the previous simulations of Alviani et al. [7] and Howerton et al. [3], the global heat transfer coefficient peak is not on the cylinder centerline. The peak value of $h/h_{ref} = 42$ shown in Fig. 24 is smaller than the peak noted from the top wall in Fig. 23. Both the IDDES cylinder and IDDES top wall heat transfer coefficient values are well above the experimental value of $h/h_{ref} = 7.5$. The cylinder face also experiences a relatively broad range of y/D values which are above the bottom wall heat transfer peak. There are additional peaks for the reattachment locations of the vorticies at the top wall junction with the cylinder and the bottom wall junction with the cylinder. The high heat transfer and pressures seen throughout the RANS and IDDES on the cylinder face reinforce the need for attention to this area in future experiments and simulations.

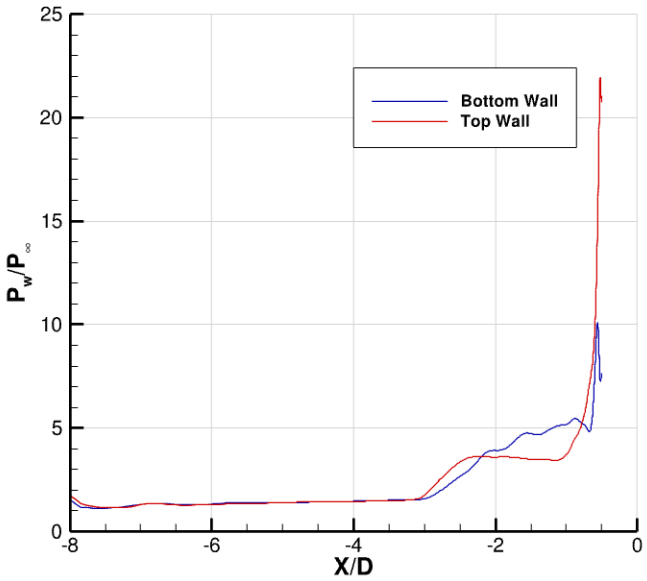

Fig. 21 IDDES pressure, centerline top and bottom plate.

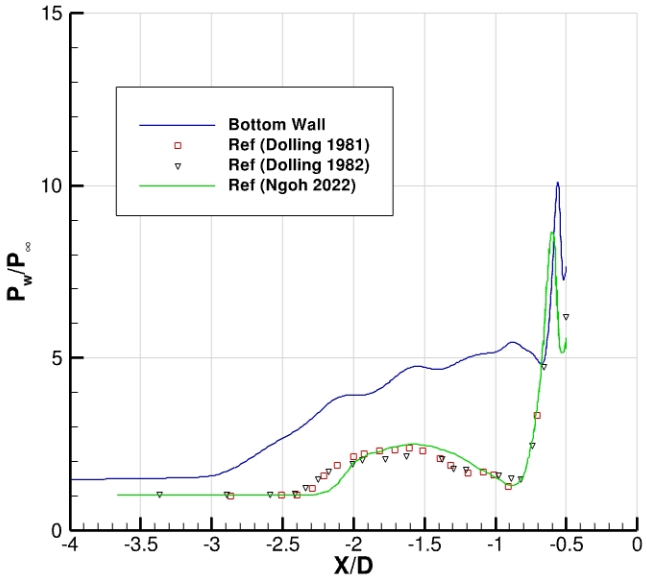

Fig. 22 IDDES pressure centerline bottom wall including experimental and computational data.

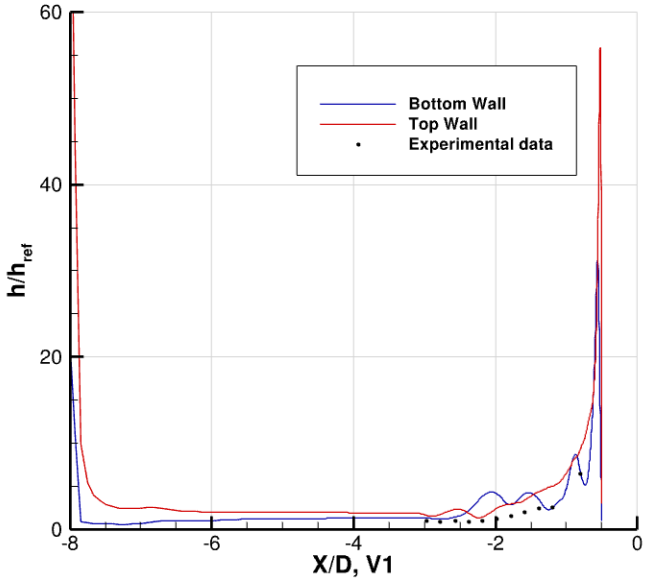

Fig. 23 IDDES heat transfer coefficient, centerline top and bottom plate.

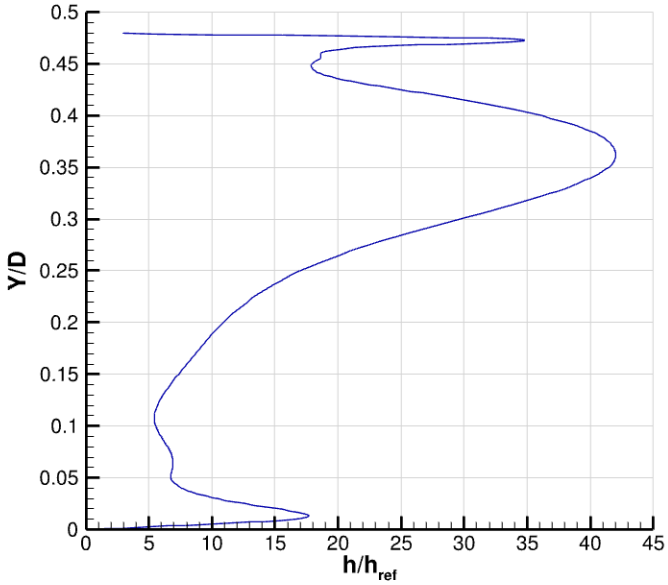

Fig. 24 IDDES heat transfer coefficient, centerline cylinder leading edge.

Power spectral density analysis is employed to determine frequencies which dominate the unsteady, complex flow. Time histories of pressure and heat fulx were collected at selected points on the walls and cylinder surface at every time step. This sampling frequency is $f_s = 10$ MHz. The MATLAB function pwelch is the implementation of Welch's method used here. The time histories were separated in 8 bins. Hamming windowing was used and there was a 50% overlap used with the bins. The Strouhal number is used to non-dimensionalize the frequencies. The Strouhal number based on cylinder diameter and freestream speed, $St_D = fD/U_\infty$ is used. The spectra are presented in the normalized

and premultiplied form $fG(f)/\sigma^2$.

Figures 25 and 26 show premultiplied power spectral density plots of surface pressure and heat flux for select locations along the walls. Figures 27 and 28 show the same quantities at select cylinder leading edge locations. The location referred to as bottom wall separation is located on the centerline upstream of the cylinder at $x/D = -2.8$, and is associated with the time-averaged furthest upstream separation point on the bottom wall. The furthest upstream separation point on the top wall at $x/D = -2.9$ is also represented. The reattachment at $x/D = -2.1$ of the first separation on the bottom wall is also examined in for the spectral content. The bottom wall points represent the points along the horizontal axis of Fig. 20 where the first separating streamline and reattaching streamline intersect the centerline. The final location represented is the top wall upstream of the cylinder on the centerline at $x/D = -2.2$. In the time-averaged streamwise skin friction coefficient, Fig. 19, this location nearly crosses $C_{fx} = 0$. The locations on the cylinder selected represent the location of minimum and maximum heat transfer coefficient per Fig. 24, with the maximum heat transfer location being the stagnation point on the cylinder.

Shock-wave/boundary layer interactions are characterized in the literature [4, 5] as often having a low frequency unsteadiness associated with a Strouhal number $St_D \approx 0.03$. Blunt and sharp fin work by Ngoh and Poggie [14, 15, 21] also found similar characteristic Strouhal numbers. The current work could be thought of as a blunt fin with a wall constrained far field above the surface. The previous work in Howerton et al. [3] found several locations in the flow had a slightly lower Strouhal number closer to $St_D \approx 0.02$. In that work, the shock system moved roughly in the streamwise direction more than a cylinder diameter upstream and downstream with a period of 1 cycle per millisecond. This large amplitude motion was not seen in the present simulations. Figure 25 shows the pressure spectra on the wall locations. There is a dominant peak which is seen in the spectra for all locations at $St_D \approx 0.04$. This peak likely corresponds to the low frequency separation bubble breathing around values of $St_D \approx 0.03$ as each of the selected points resides at the edge of a boundary layer separation bubble induced by a shock-wave/boundary-layer interaction. The largest peak with a $St_D \approx 0.13$ comes from the location on the top wall which is nearly separated in the time average. This frequency might correspond with a temporary reattachment at that location. The peak is also seen to smaller extent in the heat transfer coefficient spectra at the same location in Fig. 26. Reattachment would increase the heat transfer rates, but pressure would likely respond faster than heat transfer thus the more dominant peak in the pressure spectra. The low frequency Strouhal number of $St_D \approx 0.04$ is also present in the heat transfer coefficient spectra.

The spectra on the cylinder do not present the classical shock-wave/boundary-layer interaction low frequency Strouhal number which is expected as the bulk of the flow is directly impinging on the surface as opposed to a shock wave. The range of Strouhal numbers is similar to the cylinder spectra seen in Howerton et al. [3]. The peak in the spectra at the location of maximum heat transfer has a value of $St_D \approx 1$. While the minimum heat transfer location does show a small pressure spectra peak at $St_D \approx 0.14$ which is very near the value seen in the largest peak in Fig. 25. Both spectra have larger tails on the distributions when compared to the wall locations. The heat transfer spectra for both cylinder locations have a slight shift to higher Strouhal numbers, but again both remain broad relative to the spectra at the wall locations. The higher Strouhal number shift comparing the cylinder values to the wall values also likely comes from the higher frequency fluctuations of the movement of the stagnation point as the shock system slightly oscillates from the combined effect of the multiple shock-wave/boundary-layer interaction separation bubbles breathing and interacting thus changing shock locations. The multiple inputs upstream might drive and oscillate the flow on the cylinder face at a higher frequency because of their interfering effects. Highly unsteady pressure and heat transfer can cause immediate as well as cyclic structural problems on aerospace vehicles. The careful design of high-speed vehicles must include shock-wave/boundary-layer interactions and their steady and unsteady effects.

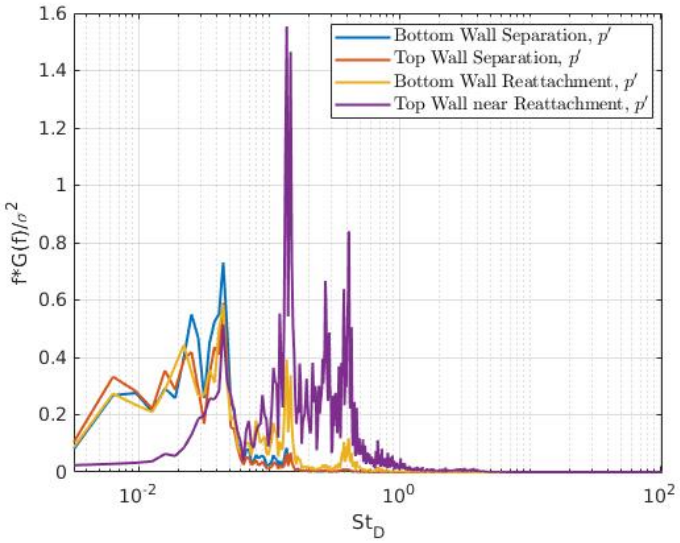

Fig. 25 Centerplane pressure spectra at selected wall locations.

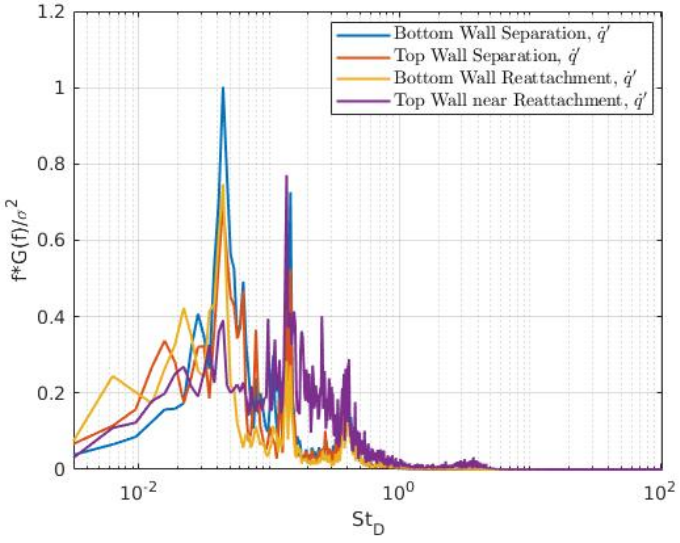

Fig. 26 Centerplane heat flux spectra at selected wall locations.

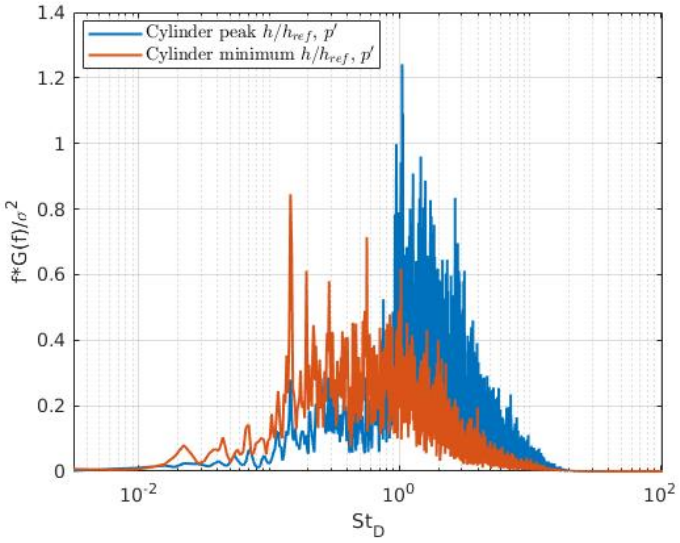

Fig. 27 Centerplane pressure spectra at selected cylinder locations.

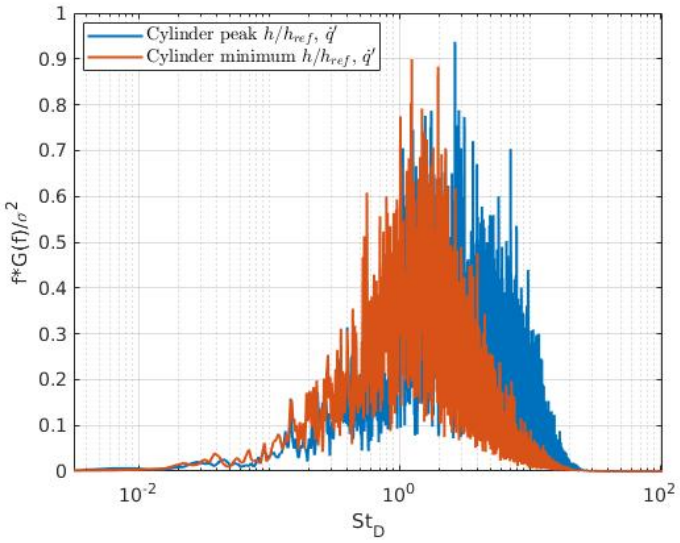

Fig. 28 Centerplane heat flux spectra at selected cylinder locations.

IV. Conclusion

Reynolds-averaged Navier-Stokes and improved delayed detached eddy simulations presented represent the a supersonic boundary layer flow ingested into a gap region. The cylinder which spans the gap produces a complex series of shock-wave/boundary-layer interactions. Mach number contours and velocity streamlines were used compare flow structure between the RANS and IDDES. The IDDES has a more complex pattern of separation bubbles compared to the RANS calculations. Streamwise skin friction coefficient and trajectories of wall skin friction were used throughout to find locations of interest in which the flow is separated from a wall. The relative increase in surface pressure and heat transfer in the interaction region compared to in the attached boundary layer is a key focus for all simulations. Peak heating and surface pressure was compared to past simulations and experiment. The peak values align much closer for the present simulations with a boundary layer inflow profile specified compared to the work in Howerton et al. [3] in which the peaks were roughly an order of magnitude higher. All simulations show the peak heat transfer on the cylinder surface or at the

junction of the cylinder surface and a wall. The increased local heating from reattachment of shock-wave/boundary-layer interaction induced separation bubbles on the walls cannot be neglected in design. The power spectral density analysis showed the low frequency Strouhal numbers associated with shock-wave/boundary-layer interactions at locations near the edges of separation bubbles. The safety, reusability, and reliability of future high-speed vehicles necessitates the continued striving for more accurate, unsteady simulations of the physics of shock-wave/boundary-layer interactions.

Acknowledgments

The presented work was supported by the U.S. Air Force Research Laboratory under the "Hypersonic Vehicle Structure Critical Technology Gaps" program, Grant Number FA8650-20-C-2407. This work is also supported in part by a grant of computer time from the DoD High Performance Computing Modernization Program at the Navy DoD Supercomputing Resource Center. The first author was supported by an NDSEG Fellowship. This material was cleared by the U.S. Air Force Research Laboratory (case number PA# AFRL-2024-6073) on 29 October 2024. Distribution Statement A: Approved for Public Release; Distribution is Unlimited.

References

[1] Stern, I., and Rowe, W. H., "Effect of gap size on pressure and heating over the flap of a blunt delta wing in hypersonic flow." *Journal of Spacecraft and Rockets*, Vol. 4, No. 1, 1967, pp. 109–114. https://doi.org/10.2514/3.28818.

[2] Cooper, L., and Putz, K. E., "Generalized Flow in Gaps and Slots Including the Effects of Ablation," *Journal of Spacecraft and Rockets*, Vol. 11, No. 5, 1974, pp. 287–294. https://doi.org/10.2514/3.62065.

[3] Howerton, L. W., Blaisdell, G., and Poggie, J., "Aerodynamic Heating of a Cylinder between Flat Plates," AIAA Paper 2024-2381, January 2024. https://doi.org/10.2514/6.2024-2381.

[4] Clemens, N. T., and Narayanaswamy, V., "Low-Frequency Unsteadiness of Shock Wave/Turbulent Boundary Layer Interactions," *Annual Review of Fluid Mechanics*, Vol. 46, No. 1, 2014, pp. 469–492. https://doi.org/10.1146/annurev-fluid-010313-141346.

[5] Gaitonde, D. V., and Adler, M. C., "Dynamics of Three-Dimensional Shock-Wave/Boundary-Layer Interactions," *Annual Review of Fluid Mechanics*, Vol. 55, No. 1, 2023, pp. 291–321. https://doi.org/10.1146/annurev-fluid-120720-022542.

[6] Neumann, R. D., and Hayes, J. R., "Aerodynamic Heating in the Fin Interaction Region of Generalized Missile Shapes at Mach 6," Tech. Rep. 79-3066, Air Force Flight Dynamics Lab, Wright-Patterson AFB, OH, 1979.

[7] Alviani, R., Fano, D., Poggie, J., and Blaisdell, G., "Aerodynamic Heating in the Gap Between a Missile Body and a Control Fin," *Journal of Spacecraft and Rockets*, Vol. 59, No. 4, 2022, pp. 1111–1124. https://doi.org/10.2514/1.A35183.

[8] Cadence Design Systems Inc., "Fidelity Pointwise User Manual," https://www.cadence.com/doc/user-manual/, Accessed 2024.

[9] Tecplot, "Tecplot 360 Version 2021r2," https://www.tecplot.com/products/tecplot-360/, Accessed 2024.

[10] The MathWorks Inc., "MATLAB version: 9.13.0 (R2022b)," https://www.mathworks.com, Accessed 2024.

[11] Department of Defense High Performance Computing Modernization Project, "HPCMP CREATE Kestrel User's Guide," https:/www.hpc.mil, Accessed 2024.

[12] Tomaro, R., Strang, W., and Sankar, L., "An implicit algorithm for solving time dependent flows on unstructured grids," AIAA Paper 1997-0333, January 1997. https://doi.org/10.2514/6.1997-333.

[13] Georgiadis, N. J., Rizzetta, D. P., and Fureby, C., "Large-Eddy Simulation: Current Capabilities, Recommended Practices, and Future Research," *AIAA Journal*, Vol. 48, No. 8, 2010, pp. 1772–1784. https://doi.org/10.2514/1.J050232.

[14] Ngoh, H., and Poggie, J., "Detached Eddy Simulation of Blunt-Fin-Induced Shock-Wave/Boundary-Layer Interaction," *AIAA Journal*, Vol. 60, No. 4, 2022, pp. 2097–2114. https://doi.org/10.2514/1.J061102.

[15] Ngoh, H., and Poggie, J., "Forced separation unsteadiness in a supersonic blunt fin flow," *Phys. Rev. Fluids*, Vol. 7, 2022, p. 093903. https://doi.org/10.1103/PhysRevFluids.7.093903.

[16] Dussauge, J.-P., Dupont, P., and Debiève, J.-F., "Unsteadiness in shock wave boundary layer interactions with separation," *Aerospace Science and Technology*, Vol. 10, No. 2, 2006, pp. 85–91. https://doi.org/https://doi.org/10.1016/j.ast.2005.09.006.

[17] Çengel, Y. A., and Ghajar, A. J., *Heat and Mass Transfer: Fundamentals and Applications*, McGraw-Hill Education, 2014, p. 26.

[18] Bernardini, M., Asproulias, I., Larsson, J., Pirozzoli, S., and Grasso, F., "Heat transfer and wall temperature effects in shock wave turbulent boundary layer interactions," *Phys. Rev. Fluids*, Vol. 1, 2016, p. 084403. https://doi.org/10.1103/PhysRevFluids.1.084403.

[19] Dolling, D., and Bogdonoff, S., "An experimental investigation of the unsteady behavior of blunt fin-induced shock wave turbulent boundary layer interaction," AIAA Paper 1982-1287, June 1981. https://doi.org/10.2514/6.1981-1287.

[20] Dolling, D., and Bogdonoff, S., "Blunt Fin-Induced Shock Wave/Turbulent Boundary-Layer Interaction," *AIAA Journal*, Vol. 20, No. 12, 1982, pp. 1674–1680. https://doi.org/10.2514/3.8003.

[21] Ngoh, H., and Poggie, J., "Upstream Forcing of Fin Induced Shock-Wave / Boundary-Layer Interactions," AIAA Paper 2023-3278, June 2023. https://doi.org/10.2514/6.2023-3278.